Thermal transfer in Rayleigh–Bénard cell with smooth or rough boundaries

E. Rusaouën[1,†]**, O. Liot**[1,‡]**, B. Castaing**[2]**, J. Salort**[1] **and F. Chillà**[1]

[1]Univ. Lyon, ENS de Lyon, Univ. Claude Bernard, CNRS, Laboratoire de Physique, F-69342 Lyon, France

[2]Univ. Grenoble Alpes, CNRS, Grenoble INP, LEGI, F-38000 Grenoble, France

Several Rayleigh–Bénard experiments in water are performed with smooth or rough boundaries. We present new thermal transfer measurements obtained with large roughness elements arranged in a square lattice. The data are compared to previous data obtained with smaller elements in the same cell (Tisserand *et al.*, *Phys. Fluids*, vol. 23, 2011). Experiments in the same apparatus without roughness are presented, as reference results, to allow for comparison. In the rough case, several regimes of heat transfer are identified: one similar to the smooth case, an enhanced heat transfer regime characterized by a modification of the Nusselt versus Rayleigh number relation and a third part where the relation can be similar to a smooth one with a corrected prefactor.

Key words: Bénard convection, convection, turbulent flows

---

1. Introduction

Turbulent Rayleigh–Bénard convection is a model system for natural convection. Theoretically, it consists of a horizontal infinite layer of fluid inserted between two plates: a hot one at the bottom and a cold one at the top. The thermal forcing sets the fluid into motion. The intensity of the forcing can be assessed by the Rayleigh number

$$Ra = \frac{g\alpha\Delta T H^3}{\nu\kappa}, \tag{1.1}$$

where ΔT is the temperature drop across the cell, H is the distance between the two plates, α is the expansion coefficient of the fluid, ν its kinematic viscosity, κ the thermal diffusivity and g the acceleration due to gravity. The fluid properties are characterized using the Prandtl number

$$Pr = \frac{\nu}{\kappa}, \tag{1.2}$$

† Present address: Univ. Grenoble Alpes, CNRS, Grenoble INP, LEGI, F-38000 Grenoble, France. Email address for correspondence: eleonore.rusaouen@ens-lyon.fr

‡ Present address: LAAS-CNRS, 7 avenue du Colonel Roche, BP54200 31031 Toulouse CEDEX 4, France.

which compares the two diffusion mechanisms that impede convection. In this work, the model experiment is a Rayleigh–Bénard cell where the layer of fluid is inserted into a cylindrical container. The only geometrical parameter is the aspect ratio $\Gamma = D/H$, where D is the diameter of the cell, and H its height.

The system response is the thermal heat flux, Q, which is larger than the case without convection. The non-dimensional heat flux is the Nusselt number, which compares the global heat flux to the purely conductive one for similar temperature drop,

$$Nu = \frac{QH}{\lambda \Delta T}, \tag{1.3}$$

where λ is the thermal conduction.

One objective is to be able to predict the thermal heat flux for a given forcing, i.e. to relate the Nusselt number to the control parameters. Several models derive predictions in the form of a scaling law,

$$Nu = \mathcal{C} Ra^a Pr^b. \tag{1.4}$$

One of the first of such models was proposed by Malkus (1954) and yields $a = 1/3$, which means that the heat flux does not depend on the distance between the plates. This is a strong indication that the plates can be described independently of one another. Many published experimental data are in fair agreement with this scaling, although there are some deviations. The reader may refer to the review of Chillà & Schumacher (2012) for more details.

An alternative description was proposed by Grossmann & Lohse (2000), where the relation is no longer a simple scaling law, but rather a superposition of scaling laws. It accounts well for the evolution of the effective scaling exponent, a, when the Rayleigh number increases. This is why it is used throughout this work to provide estimates of reference Nusselt numbers in the case of hydrodynamically smooth plates.

For asymptotically large forcings, one may expect the boundary layer to become fully turbulent, which yields $a = 1/2$ (Kraichnan 1962; Grossmann & Lohse 2011). This exponent is also a rigorous upper bound (Goluskin & Doering 2016), and the corresponding regime is sometimes called ultimate regime of convection, as there could not be a more efficient regime beyond. Several groups have claimed to observe this regime at very large Rayleigh numbers, using cryogenic gaseous helium (Chavanne *et al.* 1997; Roche *et al.* 2010), or compressed sulphur hexafluoride (He *et al.* 2012).

In this paper, we consider the case of a Rayleigh–Bénard cell with rough boundaries. The addition of a controlled roughness on the boundaries produces an enhancement of the heat transfer beyond a critical Rayleigh number, Ra_c, determined by the roughness size. Indeed, below this critical value, the thermal boundary layer is larger than the typical roughness size, and the boundary is hydrodynamically smooth. Enhancement is observed when the boundary layer thickness is the size of the roughness.

In the past, several types of enhancement have been reported. Roche *et al.* (2001*a*), Qiu, Xia & Tong (2005), Tisserand *et al.* (2011) and, in some configurations, Wei *et al.* (2014) observe an increase of the scaling law exponent a: before the transition to Nusselt enhancement, a is close to 2/7 or 1/3 then it increases and reaches nearly 1/2. In several other configurations, the exponent a is unchanged but the prefactor $\mathcal{C}$ increases (Du & Tong 1998; Wei *et al.* 2014).

In our previous works, we showed that roughness triggers turbulent instabilities in the boundary layers at moderate Rayleigh numbers (Salort *et al.* 2014) and enhance the velocity fluctuations (Liot *et al.* 2017). The objective is to gain insights into the role of turbulence on the thermal transfer, at a given Rayleigh number, hence without the need for non-conventional working fluids.

Roughness can be added to only one of the horizontal plates (Ciliberto & Laroche 1999; Tisserand *et al.* 2011; Wei *et al.* 2014), to both plates (Du & Tong 1998, 2000; Qiu *et al.* 2005) or even to the entire cell (Roche *et al.* 2001a). Several geometries of structure are used such as square pyramids, (Du & Tong 1998, 2000), pyramidal grooves (Roche *et al.* 2001a), spheres (Ciliberto & Laroche 1999) or square structures (Tisserand *et al.* 2011). Among these experiments, that of Ciliberto and Laroche does not directly compare because the roughness elements are glass spheres coated with copper varnish, so they can be considered as thermally insulating the plate. Although the details of the roughness geometry are of high interest for optimization purposes (García *et al.* 2012), we focus on the effects of roughness-triggered turbulence in general.

Recently, Toppaladoddi, Succi & Wettlaufer (2017) and Zhu *et al.* (2017) focused on the influence of the density of roughness structures on the thermal transfer. To do so, they performed several two-dimensional numerical simulations in a Rayleigh–Bénard system with sinusoidal roughness on both plates. Both studies report the dependency of the exponent a with $\Lambda = d/H$, the 'wavelength' associated with the roughness horizontal dimensions, and the existence of an optimal wavelength value, Λ_{opt}, at which a is maximum. Above Λ_{opt}, a recovers the smooth case value. Horizontal spacing was also identified as an important parameter in studies involving roughness in wind tunnel such as Perry, Schofield & Joubert (1969).

Recent experiments from Xie & Xia (2017) also evidence this role of roughness geometry. They have varied the roughness aspect ratio, λ, defined as the height of a single roughness element over its base, and found that the asymptotic scaling law exponents increase with λ. However, the roughness density also increases when λ increases, so it is not yet possible to disentangle the effect of aspect ratio and the effect of roughness density.

They evidence two transitions in the *Nu* versus *Ra* scaling: the first transition occurs when the thermal boundary layer thickness is the height of the roughness, consistent with past experiments. They call this regime of enhanced heat transfer 'Regime II'. Then, a second transition occurs when the velocity boundary layer thickness is the height of the roughness, yielding 'Regime III'. The scaling exponent in Regime III is lower than in Regime II.

In the present paper, new heat transfer measurements are presented in several rough configurations. We observe both the regime of enhanced scaling exponent a, and the regime of enhanced prefactor C. Because the roughness aspect ratio is fixed ($h_0/d = 0.4$), we cannot disentangle the role of roughness height from the role of the roughness wavelength.

After a description of the experimental apparatus, in §2, we will detail some reference results obtained in the classical smooth configuration of the cell, §3. Then, we will present the new results obtained in the rough cell with larger roughness elements and compare them to other published measurements, §4. This allows us to explore the thermal behaviour of the cell when the height of the thermal boundary layer is significantly smaller than the height of the elements.
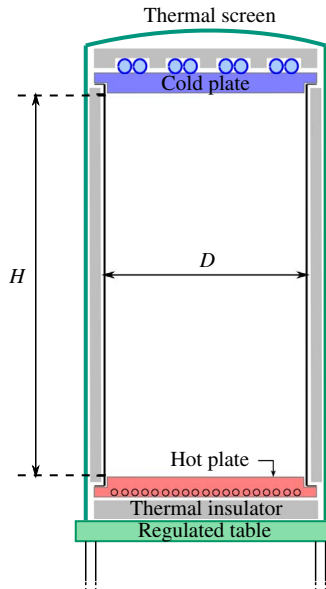
FIGURE 1. (Colour online) Sketch of the $\Gamma = 0.5$ Rayleigh–Bénard cell. Two aspect ratios can be used: $\Gamma = 0.5$ corresponding to a diameter $D = 50$ cm and a height $H = 1$ m, and $\Gamma = 2.5$ with $D = 50$ cm and $H = 20$ cm.

2. Experimental apparatus

2.1. *The cell*

The experimental apparatus consists of a cylindrical Rayleigh–Bénard cell: see figure 1. The diameter D is 0.5 m. Two sidewalls can be installed, one of height 20 cm, the second of height 1.0 m. They are made of 3 mm thick stainless steel. Figure 1 sketches the 1 m high cell, 'tall cell' ($\mathcal{TC}$), of aspect ratio $\Gamma = 0.5$. The smaller configuration, 'small cell' ($\mathcal{SC}$), has an aspect ratio $\Gamma = 2.5$.

The cold plate is made of copper coated with a thin layer of nickel to prevent chemical attack from the working fluid, deionized and degassed water. It is thermalized by a water circulation on its top which is controlled by a regulated bath. The hot plate is made of aluminium. It is heated by Joule effect using a spiralled resistor of 13 Ω inserted into the plate.

The cell is covered by a thermal insulator, 4 cm thick neoprene foam, and enclosed into a thermal screen made of copper. The mean temperature of the screen is regulated at the bulk temperature by a water bath to prevent interaction between the cell and the environment. The entire apparatus is placed on a table whose temperature is also regulated at the bulk temperature.

2.2. *Measurement techniques*

Measurements are focused on thermal transfer. To do so, the cell is instrumented with different kinds of thermometers. Six resistance temperature detectors (Pt100 type), three per plate, measure the absolute value of the temperature of each plate. Six thermocouple junctions measure the temperature at mid-height and the temperature of the bottom plate relative to the top plate with high accuracy. The common reference is then inserted into the cold plate which provides the relative zero value in the system

(T_c). Another junction is also introduced into this plate at a different radius. Two junctions are placed into the hot plate, and provide the hot temperature T_h. As the thin lateral walls are in stainless steel, they are thermalized at the bulk temperature T_b. Two junctions are then placed onto those walls to access T_b. We also measure the temperature of the thermal screen and the table. The thermocouple junctions are connected to an electronic amplifier with negligible offset. The signal is amplified 2000 times. One measurement consists of averaging over several hours (typically 48 h) of recording.

By varying the bulk temperature of the fluid, we induce variations of the fluid properties and consequently of the Prandtl number. We perform measurements at fixed Prandtl number by keeping the bulk temperature constant. This allows us to check the potential influence of the Prandtl number in a range of values between 2.5 and 6.5.

2.3. *Non-Boussinesq and lateral wall corrections*

Since our experimental procedure is similar to the one used by Tisserand *et al.* (2011), we will use the same corrections, as detailed below. First, we take care of the non-Boussinesq (NOB) effects and we show that they are negligible in our case. The Boussinesq approximation assumes that all the physical properties of the fluid are independent of the temperature except the density ρ in the buoyancy term, which can be approximated as $\rho = \rho_0(1 - \alpha \Delta T)$, where ρ_0 is the density of water at the temperature T_b. Experiments performed by Ahlers *et al.* (2006) suggest that, in water, the main sources of NOB effects are the variation of kinematic viscosity ν and thermal diffusivity κ only. In liquid water, the second one is nearly constant which leaves only the effects of ν. Ahlers *et al.* (2006) define a parameter χ, as previously done by Wu & Libchaber (1991), corresponding to the dissymmetry of the system,

$$\chi = \frac{T_h - T_b}{T_b - T_c} = 1 - c_2 \Delta T. \tag{2.1}$$

Tisserand *et al.* (2011) used a logarithmic dependence of c_2 on Prandtl number but no dependence on Rayleigh number.

$$c_2 = -0.061 Pr^{0.25} \frac{\mathrm{d}\ln(\nu)}{\mathrm{d}T}. \tag{2.2}$$

This results in corrective prefactors for the Nusselt number such as $Nu_s^{cor} = (1 + c_2 \Delta T_s/2)Nu_s$. The deviation remains smaller than 1% in all our experimental conditions, and thus can be neglected. This was also suggested by Ahlers *et al.* (2006). In their study, they performed thermal transfer measurements in water, reaching a difference of temperature of nearly 40 K, and found only small deviation of the Nusselt number from the Oberbeck–Boussinesq case. In the experiment presented here, the largest temperature difference is 20 K and the highest Rayleigh number we can attain is 1.5×10^{12}. We thus do not expect NOB corrections to be large in these conditions.

The second effect we have to consider is the spurious heat conduction in the sidewalls; see Ahlers (2000) and Roche *et al.* (2001*b*). The thermal conductivity of these walls has to be taken into account. It behaves as if the effective surface, S_{eff}, of the horizontal plates was larger than the real one S. S_{eff} can be related to S by $S_{eff} = (1 + f(W))S$, where W balances the heat conductivity of the sidewalls with the value for water and is close to 0.5, and the corrected Nusselt number is

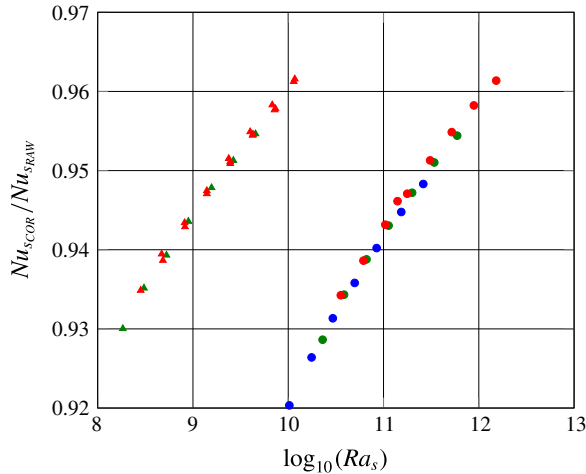$$Nu^{cor} = Nu^{raw}(1 + \mathrm{f}(W))^{-1}. \tag{2.3}$$

FIGURE 2. (Colour online) Corrective prefactors induced by sidewall effects for a smooth plate (for more details on the definitions of Nu_s and Ra_s see expressions (4.3)). Circles are for the $\mathcal{TC}$ cell and triangles are for $\mathcal{SC}$. Red refers to series at mean temperature 60 °C, green is for 40 °C and blue for 30 °C.

It yields to corrective prefactors shown in figure 2 for a smooth plate. The corrections for the rough plate are expressed in Tisserand *et al.* (2011), and we shall use the same here.

3. Reference smooth cell

Before presentation of the results obtained in the asymmetric rough cell, we shall discuss the behaviour of $\mathcal{TC}$ in the classical configuration where all boundaries are smooth. Indeed, those results were briefly discussed only in the review of Chillà & Schumacher (2012), but no detailed presentation is available in the literature. The reference case will be referred to as the '$\mathcal{RSC}$' case for 'reference smooth cell' in the following.

The experimental apparatus is the same as that described in § 2 except that the two plates are smooth, made of copper and coated with a thin layer of nickel. Results are presented in figure 3(*a*,*b*). Figure 3(*a*) shows the Nusselt number compensated by the Rayleigh number as

$$\frac{Nu}{Ra^{1/3}}. \tag{3.1}$$

The $\mathcal{RSC}$ points are shown as full black diamonds in this figure. This presentation allows us to evaluate the potential departure from a $Ra^{1/3}$ behaviour. Other results obtained in other cells are also shown for comparison. The open triangles are for Chavanne *et al.* (2001), a cylindrical cell of gaseous cryogenic helium. Green open diamonds and half-diamonds are for Niemela *et al.* (2000), in a cylindrical cell filled with gaseous helium. Violet circles are for the smooth/smooth values of Du & Tong (2000), in cylindrical cell filled with water at ambient temperature. Finally, blue stars are for Urban, Musilova & Skrbek (2011), in a cylindrical cell filled with gaseous cryogenic helium. The black line is the Grossmann–Lohse model (GL model in the following) fitted for $Pr = 3.7$. The present evaluation of Nu_{GL} is performed using the
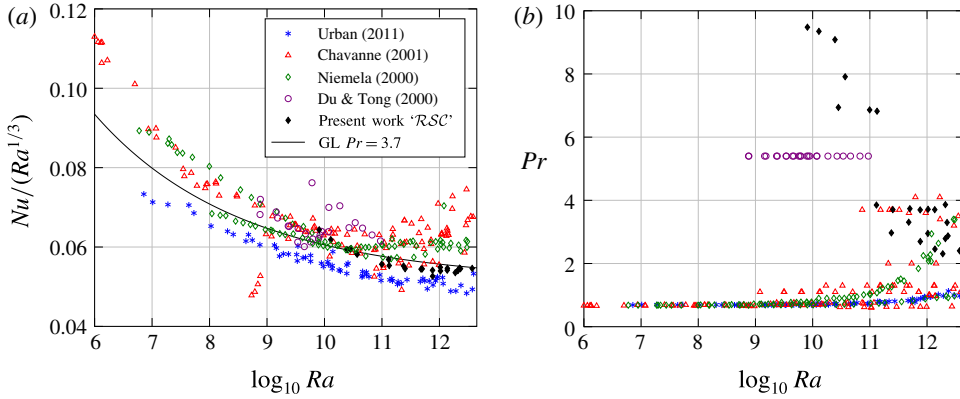
FIGURE 3. (Colour online) (*a*) Compensated Nusselt number as a function of the Rayleigh number. The symbols are the same as in (*b*). The continuous black line is the Grossmann–Lohse model with $Pr = 3.7$. The present points are represented by the full black diamond. (*b*) Prandtl number as a function of Rayleigh number.

Pr	Ra	Nu	Pr	Ra	Nu
9.48	8.10×10^9	129	2.97	1.37×10^{12}	601
9.35	1.27×10^{10}	145	3.31	1.04×10^{12}	547
9.09	2.46×10^{10}	173	3.70	7.61×10^{11}	481
7.91	3.70×10^{10}	194	3.72	2.38×10^{11}	342
6.94	2.82×10^{10}	181	3.86	4.79×10^{11}	426
6.82	1.34×10^{11}	283	2.46	2.09×10^{12}	692
6.86	9.93×10^{10}	258	2.95	1.37×10^{12}	607
3.70	7.58×10^{11}	494	3.30	1.03×10^{12}	555
3.74	5.01×10^{11}	433	2.87	2.24×10^{12}	716
3.71	2.53×10^{11}	345	2.31	3.71×10^{12}	846
3.85	1.30×10^{11}	288	2.79	2.32×10^{12}	722
2.70	1.88×10^{12}	661	2.40	3.01×10^{12}	791

TABLE 1. Values of Nusselt, Rayleigh and Prandtl numbers obtained in the $\mathcal{RSC}$, with smooth boundaries.

updated prefactors proposed by Stevens *et al.* (2013), as will be the case in the entire paper. Comparison with other experiments also shows a global collapse of all the cells. Some points from Chavanne's experiment exhibit a departure from other experiments at $Ra > 10^{12}$. The present experiment does not exhibit such a departure even at similar Rayleigh and Prandtl numbers.

Figure 3(*b*) shows the same experiments in a (Ra, Pr) phase diagram. Several points of $\mathcal{RSC}$ have no overlap with previous measurements in this (Ra, Pr) plane, and thus extend the explored parameter space. Although not all published data are shown, to our knowledge, the $\mathcal{RSC}$ data are the only data which range from $Ra = 10^{10}$ to $Ra = 10^{11}$ and $Pr > 6$. The corresponding values of the Nusselt, Rayleigh and Prandtl numbers are given in table 1.

As the GL model is in fair agreement with all the smooth experiments, and well captures the changes of behaviour in this range of Rayleigh number, we shall use its evaluated Nusselt number to normalize our results in the following and then allow for comparison.
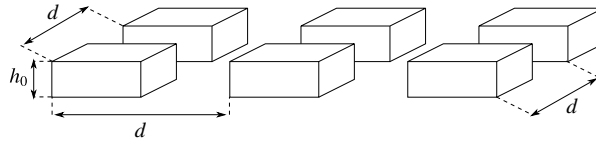
FIGURE 4. Sketch of the roughness pattern. In the present paper, results are obtained using $h_0 = 4$ mm, $d = 10$ mm with a periodicity $2d = 5h_0$. In Tisserand *et al.* (2011), $h_0 = 2$ mm and $d = 5$ mm.
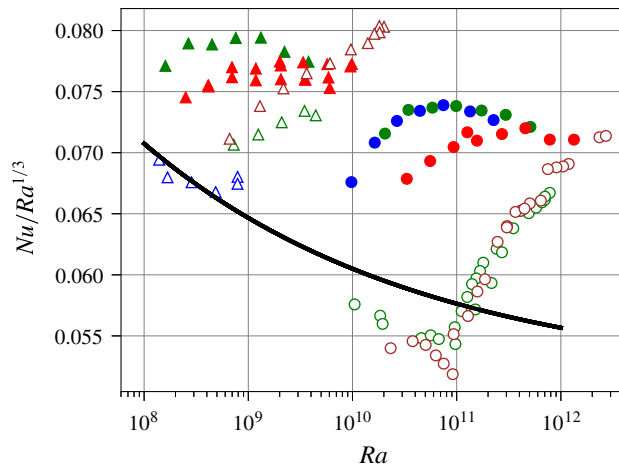

FIGURE 5. (Colour online) Global heat transfer measurements in asymmetric cells with a rough bottom plate and a smooth top plate. Colours refer to the bulk temperature T_b, blue is 25 °C or 30 °C, green is 40 °C, red 60 °C and brown 70 °C. Open symbols refer to the $h_0 = 2$ mm of Tisserand *et al.* (2011), full symbols to the current $h_0 = 4$ mm elements. Triangles are for $\mathcal{SC}$, circles for $\mathcal{TC}$. Solid line: Grossmann–Lohse model for symmetric Rayleigh–Bénard cells with smooth boundaries.

4. Convection cell with rough boundaries

In this section, we consider a rough cell, where roughness is added to the bottom plate only. The top plate and the lateral walls are smooth. The smooth plate is the same as that used for the $\mathcal{RSC}$ case previously mentioned. The symmetry is broken, the thermal impedance at the top and bottom boundaries are no longer identical, even within the Boussinesq approximation. This allows *in situ* comparison of rough and smooth boundary layers.

The roughness elements consists of cubic square studs, arranged in a lattice, as shown in figure 4. The height of the roughness elements is $h_0 = 4$ mm, their width is $d = 10$ mm. The periodicity of the pattern is $2d$. They are machined directly into the plate to preserve the thermal properties of the material. This configuration is similar to that of Tisserand *et al.* (2011), but with larger roughness elements. They used elements with $h_0 = 2$ mm and $d = 5$ mm arranged in the same way, so there is a scaling factor of 2 between the two roughness sizes. The present results will be compared with those obtained in this previous study.

It is always formally possible to define global Rayleigh and Nusselt numbers in this cell. As shown in figure 5, the global Nusselt number is larger than in the case of
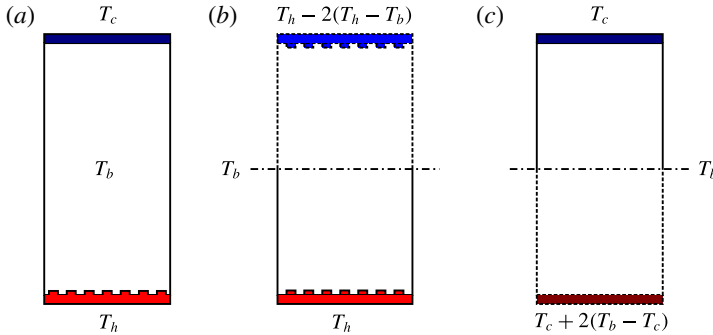
FIGURE 6. (Colour online) Separation of plates. (*a*) Asymmetric cell, (*b*) symmetric cell based on the hot plate, (*c*) symmetric cell based on the cold plate.

smooth boundaries, and the scaling exponent is modified. However, due to the mixed nature of the boundaries, and the broken symmetry, it is hard to draw more precise conclusions from these quantities.

4.1. *Separation of plates*

Following the approach of Tisserand *et al.* (2011), the asymmetric cell can be divided into two symmetric half-cells, under the assumption that the plates are independent. This procedure is justified only by the broken symmetry of the cell geometry. Indeed, although this has recently triggered some discussion (Skrbek & Urban 2015; Shishkina, Weiss & Bodenschatz 2016), its relevance as a means to recover from the non-Boussinesq effect is not discussed in this paper because our working conditions are all chosen in a range where the Boussinesq approximation holds. The bulk temperature is not equal to $(T_h + T_c)/2$ due to the impedance adaptation of the flow induced by the introduction of roughness on only one plate of the cell. The heat flux is imposed at the hot plate and the cold one is temperature regulated, which allows the bulk and hot temperatures to stabilize at free values corresponding to the stationary state of the operating point. The asymmetric cell with roughness on the bottom and without roughness on the top is sketched in figure 6(*a*). We measure T_c, T_b and T_h. If we focus on the hot/rough plate and its corresponding half-cell, we can construct the symmetrical part by considering that, with respect to the Boussinesq approximation, the corresponding cold plate should be at the temperature $T_h - 2(T_h - T_b)$: see panel (*b*). This can be done also for the cold plate, resulting in the case shown in panel (*c*). We then compute a difference of temperature corresponding to cases (*b*) and (*c*),

$$\Delta T_r = 2(T_h - T_b), \quad \Delta T_s = 2(T_b - T_c), \quad (4.1a,b)$$

and the Rayleigh and Nusselt numbers for the rough half-cell, Ra_r and Nu_r, and for the smooth half-cell, Ra_s and Nu_s,

$$Ra_r = \frac{\alpha g \Delta T_r H^3}{\nu \kappa}, \quad Nu_r = \frac{QH}{\lambda \Delta T_r}, \quad (4.2a,b)$$

$$Ra_s = \frac{\alpha g \Delta T_s H^3}{\nu \kappa}, \quad Nu_s = \frac{QH}{\lambda \Delta T_s}. \quad (4.3a,b)$$

This way, the behaviour of each plates can be characterized separately.

H (m)	Pr	Ra_{global}	Nu_{global}	Ra_s	Nu_s	Ra_r	Nu_r
1.0	5.32	1.34×10^{11}	3.76×10^2	1.54×10^{11}	3.26×10^2	1.15×10^{11}	4.44×10^2
1.0	5.44	7.46×10^{10}	3.11×10^2	8.47×10^{10}	2.72×10^2	6.44×10^{10}	3.63×10^2
1.0	5.45	4.44×10^{10}	2.60×10^2	4.98×10^{10}	2.30×10^2	3.90×10^{10}	2.99×10^2
1.0	5.45	2.67×10^{10}	2.17×10^2	2.94×10^{10}	1.96×10^2	2.40×10^{10}	2.43×10^2
1.0	5.46	1.64×10^{10}	1.80×10^2	1.76×10^{10}	1.66×10^2	1.51×10^{10}	1.96×10^2
1.0	5.45	9.76×10^9	1.44×10^2	1.03×10^{10}	1.36×10^2	9.22×10^9	1.54×10^2
1.0	5.36	2.26×10^{11}	4.43×10^2	2.61×10^{11}	3.80×10^2	1.91×10^{11}	5.30×10^2
1.0	4.37	1.74×10^{11}	4.10×10^2	2.00×10^{11}	3.53×10^2	1.47×10^{11}	4.88×10^2
1.0	4.37	9.88×10^{10}	3.41×10^2	1.13×10^{11}	2.96×10^2	8.47×10^{10}	4.03×10^2
1.0	4.36	5.84×10^{10}	2.86×10^2	6.63×10^{10}	2.50×10^2	5.06×10^{10}	3.34×10^2
1.0	4.37	3.44×10^{10}	2.39×10^2	3.85×10^{10}	2.12×10^2	3.03×10^{10}	2.74×10^2
1.0	4.38	2.05×10^{10}	1.96×10^2	2.29×10^{10}	1.74×10^2	1.81×10^{10}	2.24×10^2
1.0	4.35	2.96×10^{11}	4.87×10^2	3.41×10^{11}	4.19×10^2	2.50×10^{11}	5.81×10^2
1.0	4.31	5.10×10^{11}	5.76×10^2	5.93×10^{11}	4.92×10^2	4.27×10^{11}	6.95×10^2
1.0	2.98	4.56×10^{11}	5.54×10^2	5.20×10^{11}	4.83×10^2	3.92×10^{11}	6.50×10^2
1.0	2.97	2.72×10^{11}	4.63×10^2	3.08×10^{11}	4.07×10^2	2.36×10^{11}	5.38×10^2
1.0	2.98	1.56×10^{11}	3.83×10^2	1.77×10^{11}	3.36×10^2	1.36×10^{11}	4.44×10^2
1.0	2.96	9.34×10^{10}	3.20×10^2	1.04×10^{11}	2.85×10^2	8.28×10^{10}	3.64×10^2
1.0	2.96	5.56×10^{10}	2.65×10^2	6.15×10^{10}	2.38×10^2	4.98×10^{10}	2.98×10^2
1.0	2.96	3.32×10^{10}	2.18×10^2	3.56×10^{10}	2.02×10^2	3.08×10^{10}	2.37×10^2
1.0	2.94	1.26×10^{11}	3.60×10^2	1.40×10^{11}	3.23×10^2	1.13×10^{11}	4.06×10^2
1.0	2.96	7.83×10^{11}	6.55×10^2	8.88×10^{11}	5.75×10^2	6.78×10^{11}	7.61×10^2
1.0	2.96	1.34×10^{12}	7.83×10^2	1.52×10^{12}	6.83×10^2	1.15×10^{12}	9.16×10^2
0.2	4.36	1.32×10^9	8.71×10^1	1.57×10^9	7.30×10^1	1.07×10^9	1.08×10^2
0.2	4.37	7.58×10^8	7.24×10^1	8.95×10^8	6.10×10^1	6.21×10^8	8.90×10^1
0.2	4.37	4.49×10^8	6.04×10^1	5.27×10^8	5.10×10^1	3.71×10^8	7.40×10^1
0.2	4.38	2.66×10^8	5.08×10^1	3.06×10^8	4.40×10^1	2.26×10^8	6.00×10^1
0.2	4.39	1.60×10^8	4.19×10^1	1.84×10^8	3.60×10^1	1.36×10^8	5.00×10^1
0.2	4.40	2.22×10^9	1.02×10^2	2.66×10^9	8.50×10^1	1.79×10^9	1.28×10^2
0.2	4.40	3.78×10^9	1.21×10^2	4.54×10^9	1.00×10^2	3.02×10^9	1.52×10^2
0.2	3.03	2.01×10^9	9.78×10^1	2.37×10^9	8.20×10^1	1.65×10^9	1.21×10^2
0.2	3.06	3.36×10^9	1.16×10^2	3.99×10^9	9.70×10^1	2.73×10^9	1.44×10^2
0.2	3.04	5.73×10^9	1.38×10^2	6.80×10^9	1.16×10^2	4.66×10^9	1.71×10^2
0.2	3.07	9.56×10^9	1.64×10^2	1.14×10^{10}	1.36×10^2	7.71×10^9	2.05×10^2
0.2	2.98	9.86×10^9	1.66×10^2	1.17×10^{10}	1.39×10^2	8.02×10^9	2.05×10^2
0.2	2.93	6.05×10^9	1.37×10^2	7.34×10^9	1.12×10^2	4.76×10^9	1.77×10^2
0.2	2.95	3.54×10^9	1.16×10^2	4.27×10^9	9.50×10^1	2.80×10^9	1.48×10^2
0.2	3.00	2.05×10^9	9.80×10^1	2.46×10^9	8.10×10^1	1.64×10^9	1.24×10^2
0.2	2.96	1.18×10^9	8.13×10^1	1.40×10^9	6.80×10^1	9.63×10^8	1.01×10^2
0.2	2.97	6.98×10^8	6.83×10^1	8.18×10^8	5.80×10^1	5.77×10^8	8.30×10^1
0.2	2.98	4.16×10^8	5.63×10^1	4.84×10^8	4.80×10^1	3.47×10^8	6.80×10^1
0.2	2.99	5.88×10^9	1.37×10^2	7.19×10^9	1.12×10^2	4.58×10^9	1.78×10^2
0.2	2.98	3.50×10^9	1.15×10^2	4.23×10^9	9.50×10^1	2.77×10^9	1.47×10^2
0.2	3.01	2.06×10^9	9.66×10^1	2.46×10^9	8.00×10^1	1.65×10^9	1.22×10^2
0.2	3.00	1.18×10^9	8.02×10^1	1.40×10^9	6.70×10^1	9.61×10^8	1.00×10^2
0.2	3.03	6.98×10^8	6.76×10^1	8.25×10^8	5.70×10^1	5.72×10^8	8.30×10^1
0.2	3.01	4.13×10^8	5.62×10^1	4.70×10^8	4.90×10^1	3.56×10^8	6.60×10^1
0.2	3.04	2.50×10^8	4.70×10^1	2.83×10^8	4.10×10^1	2.18×10^8	5.50×10^1

TABLE 2. Heat transfer data in the asymmetric cells with rough bottom plate and smooth top plate.
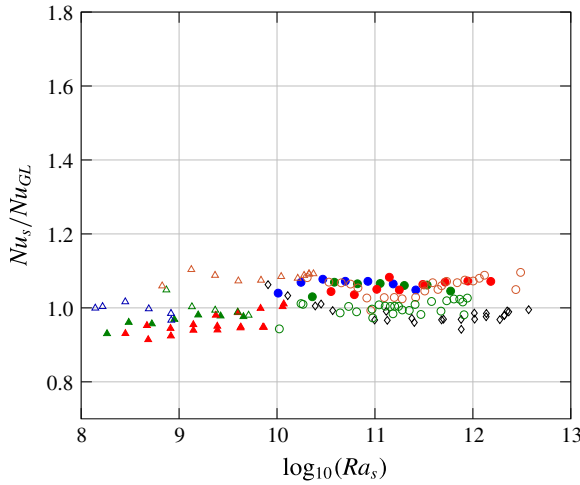
FIGURE 7. (Colour online) Thermal transfer of the smooth plate: Nu_s normalized by the Grossmann–Lohse model computed with respect to the experimental Prandtl number as a function of Ra_s. Colours refer to the bulk temperature T_b, blue is 25 °C or 30 °C, green is 40 °C, red 60 °C and brown 70 °C. Open symbols refer to the $h_0 = 2$ mm case of Tisserand *et al.* (2011), full symbols to the current $h_0 = 4$ mm elements. Triangles are for $\mathcal{SC}$, circles for $\mathcal{TC}$. Black diamonds are for the reference smooth/smooth cell presented in § 3.

4.1.1. *Smooth plate case*

Let us first consider the smooth plate. In our previous work (Tisserand *et al.* 2011), the thermal transfer of the smooth plate was not modified by the presence of the roughness on the hot plate. To verify that this still holds in the case of larger roughness elements, the Nusselt number of the smooth half-cell is plotted in figure 7.

Four sets of points are presented, obtained for the tall and small cells, and each with two roughness sizes. These four experimental configurations are compared to the $\mathcal{RSC}$ configuration previously discussed in § 3 (black open diamonds on figure 7). We then can discuss four different experimental configurations compared to the reference points. Open triangles and circles correspond to Tisserand *et al.* (2011), for aspect ratios $\Gamma = 2.5$ and $\Gamma = 1/2$ respectively, colours are Prandtl number series: blue for $T_b = 25$ °C, green for $T_b = 40$ °C and brown for $T_b = 70$ °C corresponding to Prandtl numbers of 6.1, 4.3 and 2.5. Full symbols are the new results presented here, blue is for $T_b = 30$ °C, red for $T_b = 60$ °C. The ordinate has been extended in order to range the same values as those of figure 8 for comparison. The Nusselt numbers of the smooth half-cells and those of the reference smooth cell collapse on a single horizontal line when compensated by the prediction from the GL model. The dispersion around the horizontal line is less than 10 %.

The thermal efficiency of the smooth/cold plate is not modified by the presence of roughness on the opposite hot plate and this is in good agreement with the reference results obtained in the fully smooth cell. This backs up the independence of the plates. Similar observations were also made by Wei *et al.* (2014) in an asymmetrical cell. The behaviour of the smooth plate was not changed by the introduction of roughness elements on the opposite plate. This was tested with roughness either on the bottom or the top plate and suggests that the independence of the plates is a robust result in the range of Rayleigh numbers explored here (Ra larger than 10^8). However, some
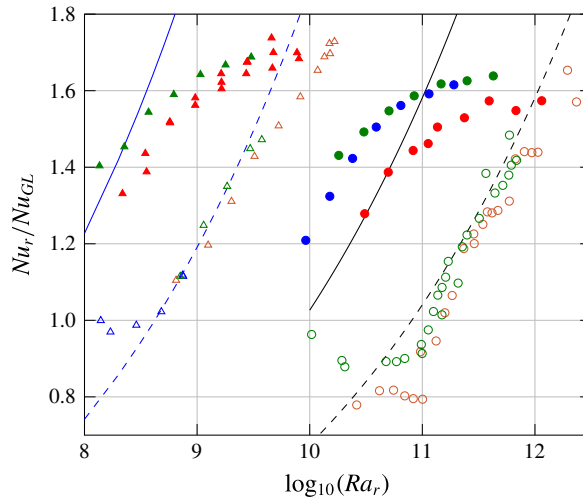
FIGURE 8. (Colour online) Thermal transfer of the rough plate: Nu_r normalized by the Grossmann–Lohse model computed with respect to the experimental Prandtl number as a function of Ra_r. Symbol and colour choices are the same as figure 7. Lines stand for expression (4.5): blue lines are $\mathcal{SC}$, black lines are $\mathcal{TC}$, full lines are for $h_0 = 4$ mm and dashed lines for $h_0 = 2$ mm.

recent particle image velocimetry (PIV) measurements (Liot *et al.* 2017) performed in an asymmetric rough cell seem to show a major increase of the root mean square of the velocity close to the smooth plate at nearly constant Rayleigh number. Although the introduction of roughness on one plate yields larger fluctuations in the bulk, it does not change the efficiency of the smooth plate.

4.1.2. *Rough plate case*

The heat transfer measurements of the rough half-cell are presented in figure 8. The four sets of points are clearly disjoined and correspond to the $\mathcal{SC}$ (low Rayleigh numbers) and $\mathcal{TC}$ (large Rayleigh numbers) and to the two sizes of roughness elements: the small one used by Tisserand *et al.* (2011) and the large one presented here. The comparison between those two plots gives another argument for the independence of the plates: the scaling law behaviour of one plate may significantly differ from the other.

The open symbols are the previous points from Tisserand *et al.* (2011), with a roughness size $h_0 = 2$ mm. The full symbols are the new measurements obtained with $h_0 = 4$ mm. Both exhibit a regime of enhanced heat transfer, with a scaling exponent a higher than the smooth case which starts when the height of the thermal boundary layer, δ_θ,

$$\delta_\theta = \frac{H}{2Nu_r}, \tag{4.4}$$

gets smaller than the roughness height, h_0, i.e. when the plate is hydrodynamically rough. That is why the Rayleigh number threshold differs for the four values of h_0/H (0.02, 0.01, 0.004, 0.002 from left to right in figure 8).

The effective scaling exponent is close to $1/2$ and the prefactor agrees fairly well with the roughness-induced turbulent structure of the boundary layer described by

σ	H	h_0
0.0607	1 m	4 mm
0.0579	1 m	2 mm
0.0740	0.2 m	4 mm
0.0667	0.2 m	2 mm

TABLE 3. Values of the parameter σ.

Salort *et al.* (2014). The lines shown in figure 8 are estimates from equation (23) of Salort *et al.* (2014),

$$Nu = \frac{(2\sigma)^{3/2}}{2} \left(\frac{h_0}{H}\right)^{1/2} Ra^{1/2}, \tag{4.5}$$

where

$$\sigma = \frac{Nu_c}{Ra_c^{1/3}}, \tag{4.6}$$

and Nu_c and Ra_c are the critical values of Nu_r and Ra_r at the transition. Because this transition is controlled by the height of the thermal boundary layer, one can write

$$Nu_c = \frac{H}{2h_0}. \tag{4.7}$$

The range of Rayleigh numbers is wider than was considered by Salort *et al.* (2014), therefore it is not possible to choose one single value for σ: typically $\sigma = 0.06$ for $Ra > 10^{11}$ where the scaling exponent is $1/3$. For lower Rayleigh numbers, the effective value of σ is larger. One way to estimate its value is to use the GL model which is well suited to yield estimates of the Nusselt number as long as the plate is hydrodynamically smooth.

Let f_{GL} be the function that gives the Nusselt number for a given Rayleigh number in the GL model, i.e.

$$Nu_{GL} = f_{GL}(Ra). \tag{4.8}$$

Then the critical Rayleigh number, Ra_c, beyond which the plate gets hydrodynamically rough can be estimated as

$$Ra_c = f_{GL}^{-1}\left(\frac{H}{2h_0}\right), \tag{4.9}$$

and therefore

$$\sigma = \frac{H}{2h_0 f_{GL}^{-1}(H/(2h_0))}. \tag{4.10}$$

The values of σ are shown in table 3. The prediction (4.5) has no free parameters: it is fully determined by the two geometrical parameters, h_0 and H. As shown in figure 9, this estimate collapses the 4 datasets onto one master curve. There is however
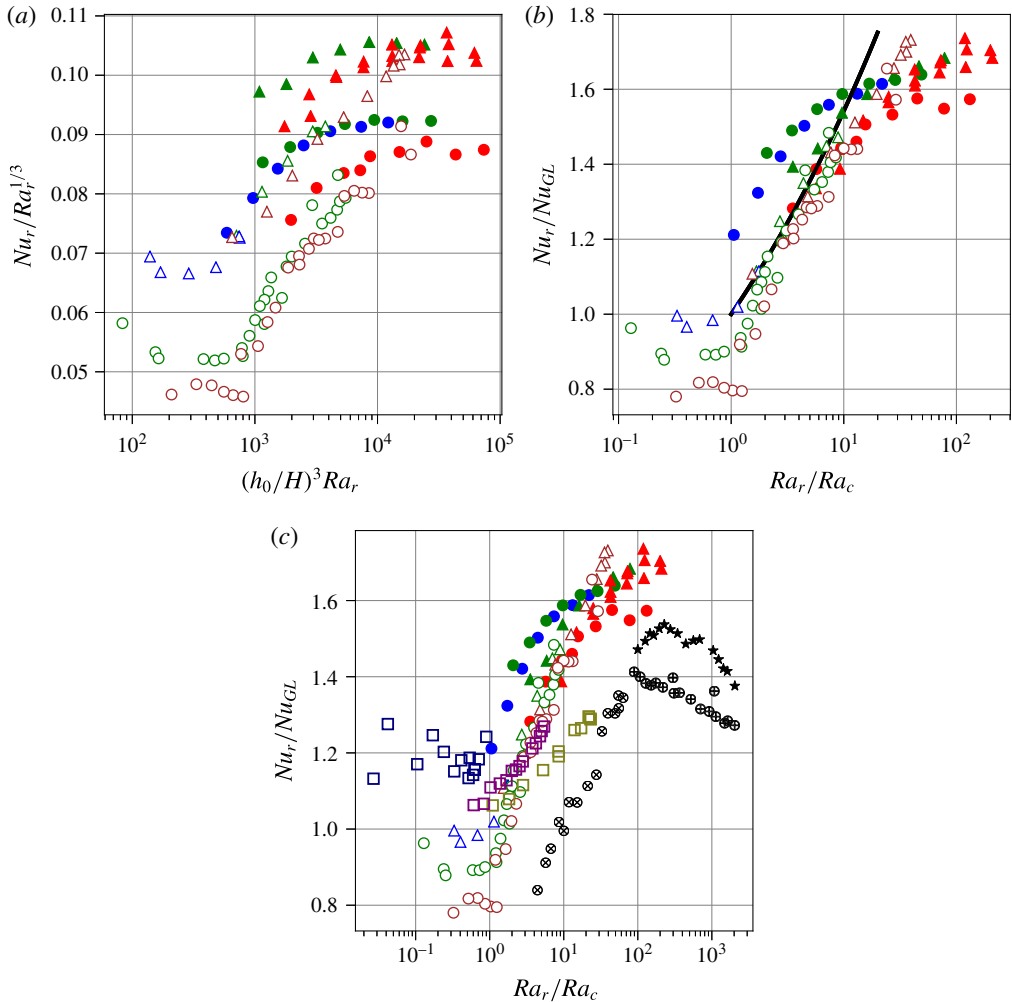
FIGURE 9. (Colour online) (*a*) Rough half-cell heat transfer measurements with $Ra^{1/3}$ compensation. Circles and triangles are data from the present work with the same conventions as in figure 7. (*b*) Rough half-cell heat transfer enhancement Nu_r/Nu_{GL} versus compensated Rayleigh number Ra_r/Ra_c. The collapse is better because the use of GL model accounts for variation of the effective exponent. Black solid line: roughness-triggered turbulent model from (4.5). (*c*) Compilation of several cell geometries. Black symbols are from the cylindrical asymmetric cell from Wei *et al.* (2014). Stars are $h_0 = 8$ mm R/S, +-circles are $h_0 = 8$ mm S/R and ×-circles are $h_0 = 3$ mm R/S. Squares are from the rectangular Rayleigh–Bénard cell from Salort *et al.* (2014).

still some dispersion left. This could be caused by the effect of the Prandtl number, which is not taken into account in this description. Recent experiments of Xie & Xia (2017) also suggest that the heat transfer efficiency in the case of rough boundaries gets larger when the Prandtl number is increased. They evidence such increase only for larger Prandtl numbers than we do, but the geometry of the cells and roughness significantly differ. Our results are consistent with theirs in the sense that the Nusselt number tends to increase with the Prandtl number in the rough configuration only.
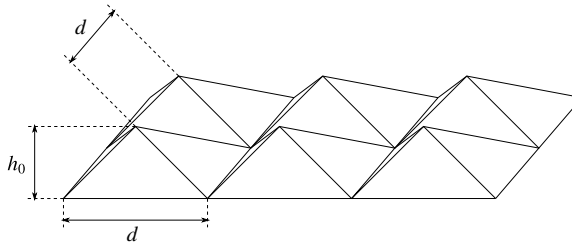
FIGURE 10. Sketch of the pyramidal roughness used by Wei *et al.* (2014).

As long as the boundary is hydrodynamically smooth, the Nusselt number does not significantly depend on the Prandtl number. However, it is possible that the velocity boundary layer thickness also plays a role near the threshold, and therefore the critical Rayleigh number may depend on the Prandtl number.

For Rayleigh numbers lower than Ra_c, the plate is hydrodynamically smooth, and the scaling exponent is similar to that of a smooth plate. However, several Nusselt numbers are lower than predicted by the GL model. This indicates that the thermal transfer is less efficient than in the classical smooth case. The interpretation proposed by Tisserand *et al.* (2011) was that it is caused by the additional thermal impedance of the fluid which fills the space around the roughness elements and locally thickens the boundary layer.

In the high Rayleigh number limit, the data exhibit a second transition, both for the tall and small cells. In this range, the heat transfer is still larger than the smooth case, and larger than effective surface increase (40 %), but the scaling exponent a is less than 1/2. It may be related to other published works which have reported an increase of the prefactor C caused by enhanced plume emissions, rather than an increase of the exponent a due to a change in the structure of the boundary layer. This seems consistent, in particular, with the recent results of Xie & Xia (2017) in their symmetric rough cell where both plates have pyramid-shaped roughness elements.

To the best of our knowledge, there are only two other published datasets in asymmetric Rayleigh–Bénard cells: Wei *et al.* (2014) and Salort *et al.* (2014). The former performed experiments in a cylinder of aspect ratio close to 1. They used pyramidal elements as roughness, sketched in figure 10. The base length d is equal to $2h_0$. The surface increase induced was 41 %. The latter uses similar square-stud roughness but within a rectangular cell with vertical aspect ratio width/height = 1 and horizontal aspect ratio depth/width = 0.25.

These datasets are shown in figure 9. As could be expected, the points do not exactly collapse. Indeed, the details of the geometry may change prefactors in the Nusselt numbers. However, the observations of the three regimes hold, the Rayleigh number thresholds are all consistent and the enhancement goes beyond the increase solely yielded by the increase of the effective surface area.

5. Discussion

Thermal transfer measurements have been carried out in a cylindrical Rayleigh–Bénard cell with square roughness on the bottom plate for two different cell aspect ratios. The results have been compared to previous studies, with different roughness shapes and dimensions. The Grossmann–Lohse model is used to estimate the Nusselt numbers when the boundaries are smooth.

We have shown that both plates are independent, at least when the thermal impedance is considered. The impedance of the smooth boundary is fully determined by its temperature difference to the bulk, and the classical scaling law is fully recovered when the Rayleigh number of the smooth half-cell is considered. Beyond a critical Rayleigh number corresponding to a thermal boundary layer smaller than the typical roughness size, the thermal impedance of the rough boundary is smaller than the smooth case, and is well described by a turbulent destabilization of the boundary layer.

Such destabilization was confirmed directly by the work of Liot *et al.* (2016) where PIV measurements have exhibited a turbulent velocity profile in the boundary layer. However, other enhancement mechanisms were also proposed in the past. In particular, Du & Tong (2000) used thermochromic liquid crystals to measure temperature fields close to a rough plate. Tips of roughness elements seemed to be preferential points of nucleation of thermal plumes. Following this hypothesis, we can assume that a cube can induce a higher increase of the thermal transfer than a pyramid since a cube is formed of four singularities (i.e. corners) interacting with the fluid whereas a pyramid only exhibits one singularity. The details of the shape of the roughness elements, such as sharp edges and vertical surfaces, surely bear some importance and may be investigated further. As can be seen in figure 9, the curves obtained with cubic roughness elements are above those obtained with pyramids, which backs up the idea that more plumes are induced by cubes than pyramids.

At lower Rayleigh numbers, Nu_r/Nu_{GL} is lower than 1 for several experiments (Tisserand *et al.* 2011; Wei *et al.* 2014). This could be caused by an additional thermal resistance induced by motionless fluid between the roughness elements, as was suggested by PIV measurements (Liot *et al.* 2016).

Though the actual Nusselt numbers depend on the details of the geometry, several observations hold for all known set-ups, regardless of the roughness or cell geometry. Like Xie & Xia (2017), three regimes can be consistently exhibited: (i) below Ra_c, $Nu_r/f_{GL}(Ra_r)$ are horizontal lines, meaning that the behaviour is similar to a smooth plate, and consistent with the GL model within $\pm 20\%$; (ii) a regime of increased scaling exponent occurs beyond Ra_c, fairly compatible with $a = 1/2$, and more precisely with (4.5), which suggests a roughness-triggered turbulent boundary layer structure; (iii) a third regime, where the heat transfer is enhanced, more than the increase of effective surface area, but the scaling exponent is lower than in the second regime, which suggests that turbulent destabilization of the boundary layer may no longer be the dominant enhancement mechanism.

Acknowledgements

REFERENCES

AHLERS, G. 2000 Effect of sidewall conductance on heat-transport measurements for turbulent Rayleigh–Bénard convection. *Phys. Rev.* E **63**, 015303.

AHLERS, G., BROWN, E., ARAUJO, F., FUNFSCHILLING, D., GROSSMANN, S. & LOHSE, D. 2006 Non-Oberbeck–Boussinesq effects in strongly turbulent Rayleigh–Bénard convection. *J. Fluid Mech.* **569**, 409–445.

CHAVANNE, X., CHILLÀ, F., CASTAING, B., HÉBRAL, B., CHABAUD, B. & CHAUSSY, J. 1997 Observation of the ultimate regime in Rayleigh–Bénard convection. *Phys. Rev. Lett.* **79**, 3648–3651.

CHAVANNE, X., CHILLÀ, F., CHABAUD, B., CASTAING, B. & HÉBRAL, B. 2001 Turbulent Rayleigh–Bénard convection in gaseous and liquid He. *Phys. Fluids* **13**, 1300–1320.

CHILLÀ, F. & SCHUMACHER, J. 2012 New perspectives in turbulent Rayleigh–Bénard convection. *Eur. Phys. J.* E **35**, 58.

CILIBERTO, S. & LAROCHE, C. 1999 Random roughness of boundary increases the turbulent convection scaling exponent. *Phys. Rev. Lett.* **82**, 3998–4001.

DU, Y.-B. & TONG, P. 1998 Enhanced heat transport in turbulent convection over rough surface. *Phys. Rev. Lett.* **81**, 987–990.

DU, Y.-B. & TONG, P. 2000 Turbulent thermal convection in a cell with ordered rough boundaries. *J. Fluid Mech.* **407**, 57–84.

GARCÍA, A., SOLANO, J. P., VICENTE, P. G. & VIEDMA, A. 2012 The influence of artificial roughness shape on heat transfer enhancement: corrugated tubes, dimpled tubes and wire coils. *Appl. Therm. Engng* **35**, 196–201.

GOLUSKIN, D. & DOERING, C. R. 2016 Bounds for convection between rough boundaries. *J. Fluid Mech.* **804**, 370–386.

GROSSMANN, S. & LOHSE, D. 2000 Scaling in thermal convection: a unifying theory. *J. Fluid Mech.* **407**, 27–56.

GROSSMANN, S. & LOHSE, D. 2011 Multiple scaling in the ultimate regime of thermal convection. *Phys. Fluids* **23**, 045108.

HE, X., FUNFSCHILLING, D., NOBACH, H., BODENSCHATZ, E. & AHLERS, G. 2012 Transition to the ultimate state of turbulent Rayleigh–Bénard convection. *Phys. Rev. Lett.* **108**, 024502.

KRAICHNAN, R. H. 1962 Turbulent thermal convection at arbitrary Prandtl number. *Phys. Fluids* **5** (11), 1374–1389.

LIOT, O., EHLINGER, Q., RUSAOUEN, E., COUDARCHET, T., SALORT, J. & CHILLÀ, F. 2017 Velocity fluctuations and boundary layer structure in a rough Rayleigh–Bénard cell filled with water. *Phys. Rev. Fluids* **2**, 044605.

LIOT, O., SALORT, J., KAISER, R., DU PUITS, R. & CHILLÀ, F. 2016 Boundary layer structure in a rough Rayleigh–Bénard cell filled with air. *J. Fluid Mech.* **786**, 275–293.

MALKUS, W. V. R. 1954 The heat transport and spectrum of thermal turbulence. *Proc. R. Soc. Lond.* A **225**, 196–212.

NIEMELA, J. J., SKRBEK, L., SREENIVASAN, K. R. & DONNELLY, R. J. 2000 Turbulent convection at very high Rayleigh numbers. *Nature* **404**, 837.

PERRY, E., SCHOFIELD, W. H. & JOUBERT, P. N. 1969 Rough wall turbulent boundary layers. *J. Fluid Mech.* **37**, 383–413.

QIU, X.-L., XIA, K.-Q. & TONG, P. 2005 Experimental study of velocity boundary layer near a rough conducting surface in turbulent natural convection. *J. Turbul.* **6**, N30.

ROCHE, P.-E., CASTAING, B., CHABAUD, B. & HÉBRAL, B. 2001a Observation of the 1/2 power law in Rayleigh–Bénard convection. *Phys. Rev.* E **63**, 045303.

ROCHE, P.-E., CASTAING, B., CHABAUD, B., HÉBRAL, B. & SOMMERIA, J. 2001b Side wall effects in Rayleigh–Bénard experiments. *Eur. Phys. J.* B **24**, 405.

ROCHE, P.-E., GAUTHIER, F., KAISER, R. & SALORT, J. 2010 On the triggering of the ultimate regime of convection. *New J. Phys.* **12**, 085014.

SALORT, J., LIOT, O., RUSAOUEN, E., SEYCHELLES, F., TISSERAND, J.-C., CREYSSELS, M., CASTAING, B. & CHILLÀ, F. 2014 Thermal boundary layer near roughnesses in turbulent Rayleigh–Bénard convection: flow structure and multistability. *Phys. Fluids* **26**, 015112.

SHISHKINA, O., WEISS, S. & BODENSCHATZ, E. 2016 Conductive heat flux in measurements of the nusselt number in turbulent Rayleigh–Bénard convection. *Phys. Rev. Fluids* **1**, 062301.

SKRBEK, L. & URBAN, P. 2015 Has the ultimate state of turbulent thermal convection been observed? *J. Fluid Mech.* **785**, 270–282.

STEVENS, R. J. A. M., VAN DER POEL, E. P., GROSSMANN, S. & LOHSE, D. 2013 The unifying theory of scaling in thermal convection: the updated prefactors. *J. Fluid Mech.* **730**, 295–308.

TISSERAND, J.-C., CREYSSELS, M., GASTEUIL, Y., PABIOU, H., GIBERT, M., CASTAING, B. & CHILLÀ, F. 2011 Comparison between rough and smooth plates within the same Rayleigh–Bénard cell. *Phys. Fluids* **23**, 015105.

TOPPALADODDI, S., SUCCI, S. & WETTLAUFER, J. S. 2017 Roughness as a route to the ultimate regime of thermal convection. *Phys. Rev. Lett.* **118**, 074503.

URBAN, P., MUSILOVA, V. & SKRBEK, L. 2011 Efficiency of heat transfer in turbulent Rayleigh–Bénard convection. *Phys. Rev. Lett.* **107**, 014302.

WEI, P., CHAN, T.-S., NI, R., ZHAO, X.-Z. & XIA, K.-Q. 2014 Heat transport properties of plates with smooth and rough surfaces in turbulent thermal convection. *J. Fluid Mech.* **740**, 28–46.

WU, X.-Z. & LIBCHABER, A. 1991 Non-Boussinesq effects in free thermal convection. *Phys. Rev.* A **43**, 2833–2839.

XIE, Y.-C. & XIA, K.-Q. 2017 Turbulent thermal convection over rough plates with varying roughness geometries. *J. Fluid Mech.* **825**, 573–599.

ZHU, X., STEVENS, R. J. A. M., VERZICCO, R. & LOHSE, D. 2017 Roughness-facilitated local 1/2 scaling does not imply the onset of the ultimate regime of thermal convection. *Phys. Rev. Lett.* **119**, 154501.